NASA-CR-204817

Processing and mechanical properties of in-situ composites from the NiAl–Cr and the NiAl–(Cr,Mo) eutectic systems

D. R. Johnson, X. F. Chen,* B. F. Oliver

The University of Tennessee, Knoxville, Tennessee 37996 2200, USA

R. D. Noebe & J. D. Whittenberger

NASA Lewis Research Center, Cleveland, Ohio 44135, USA

In-situ composites based on the NiAl Cr eutectic system have been successfully produced by containerless processing and evaluated. Molybdenum additions of 0·6 to 6 at.% were used to change the eutectic microstructure. The NiAl Cr alloys had a fibrous microstructure, while the NiAl–(Cr,Mo) alloys containing 1 at.% or more of molybdenum exhibited a lamellar structure. The room temperature fracture toughness of the different eutectic alloys was evaluated. The toughness values of the directionally solidified eutectics were similar regardless of composition or eutectic morphology, but all the directionally solidified alloys exhibited superior toughness compared to binary NiAl or conventionally cast eutectics. However, the principal mechanism responsible for the improved toughness of the directionally solidified alloys was dependent on the second phase morphology. The effect of eutectic morphology on the 1300 K creep strength was also investigated by testing a typical fiber reinforced and a lamellar reinforced eutectic. A molybdenum-doped alloy with the lamellar eutectic morphology exhibited the best creep resistance. Due to the promising creep behavior of this NiAl 28Cr 6Mo alloy at 1300 K, additional creep testing was performed at 1200 and 1400 K. This NiAl (Cr,Mo) eutectic displays promising high temperature strength while still maintaining a reasonable room temperature fracture toughness when compared to other NiAl-based eutectics.

Key words: in-situ composites, NiAl Cr, NiAl (Cr, Mo), directional solidification, eutectic morphology, creep resistance.

1 INTRODUCTION

Nickel aluminide (NiAl) has a number of attractive properties including excellent oxidation resistance, high melting temperature, high thermal conductivity and relatively low density. As a result, alloys based on the intermetallic compound NiAl are being considered as candidate materials to replace nickel-based superalloys in some high temperature structural applications.[1] While NiAl possesses many advantageous properties, currently it is not used in load bearing applications due to inadequate low temperature fracture toughness

and poor elevated temperature strength. Alloying NiAl to form in-situ composite materials may be one way to improve both of these properties.

For instance, ductile phase toughening is one method for improving the fracture resistance and ductility of brittle materials. Increased toughness is provided by the interaction between the propagating crack and the ductile phase during the fracture process. The challenge is to increase the toughness and at the same time improve the high temperature strength of the intermetallic compound. For example, introducing Ni_3Al as a ductile phase in NiAl improves the ductility and toughness of the composite material over that of binary NiAl. Unfortunately, the effective melting point is depressed and the creep strength of the two-phase alloys, depending on the

*Visiting scholar from Materials Science Department, Shanghai Jiao Tong University, People's Republic of China.

specific composition, is about the same or less than that of binary NiAl.[2]

On the other hand, a number of eutectic alloys consisting of NiAl and a refractory metal phase, such as NiAl–Cr, show both improved toughness and creep strength compared to single-phase NiAl.[3–6] Directional solidification of these eutectic alloys results in in-situ composites where one or more phases are aligned parallel to the growth direction. In this case, the reinforcing refractory metal phase provides increases in both the toughness and creep strength of the composite material.

One advantage of producing composites by directional solidification of eutectic alloys is that the phases are thermodynamically stable even up to the melting point. A disadvantage is that alloy compositions are limited by the appropriate phase equilibria needed for eutectic growth. In many systems these compositions are often unknown.

Fortunately, the NiAl–Cr system is well characterized in terms of processing–microstructure relationships, second phase morphology and constitutional associations.[3,6,10] The morphology of the NiAl–34Cr (atomic percent) eutectic consists of chromium rods within a NiAl matrix, both having a <100> growth orientation. The early work by Cline and Walter[7] has shown that small additions of impurity elements such as Mo, V and W will change the growth direction to <111> for both phases, while changing the microstructure to a lamellar morphology. For example, additions of molybdenum greater than 0·6 at.% will result in a lamellar chromium morphology with a {112} facet plane. Thus, the effects of second phase morphology and the orientation of the reinforcing phase may be studied without large changes in the volume fraction of reinforcement.

While the microstructures of these NiAl–(Cr,X) alloys have been characterized, mechanical property data are sparse. Furthermore, processing procedures and resulting microstructures generally vary with each investigator, making comparisons between research groups difficult. Therefore, the purpose of this study was to characterize the effects of containerless processing (described below) on the microstructure and subsequently the fracture toughness and elevated temperature strength of in-situ composites based on the NiAl–Cr and NiAl–(Cr,Mo) eutectic systems. Emphasis was placed on producing high purity material of low interstitial content by containerless processing.[11] Finally, the properties of these alloys were compared to the properties of other eutectic systems that were processed under similar conditions.[5]

2 PROCESSING AND MATERIALS

Directional solidification of near-eutectic alloys was used to produce in-situ composites with aligned microstructures for mechanical testing. Precursor ingots consisting of the NiAl–Cr eutectic and those alloyed with molybdenum were produced by induction melting of elemental Ni, Al, Mo and a Ni–Cr master alloy. The 1 kg charge was then chill cast into a copper mold. After removal of the hot-top, precursor ingots were nominally 25 mm in diameter and 300 mm in length. These ingots were then directionally solidified in the containerless mode by the electromagnetically levitated zone process in an ultrapure helium atmosphere.

Containerless processing offers the advantage of enhanced purity by eliminating the possibility of alloy contamination from the crucible. The crucible is eliminated by using induction power to heat, levitate and constrain the liquid zone. The method for producing the electromagnetically constrained liquid zone is shown in Fig. 1. To allow for volume expansion upon melting, a gap is left between the upper and lower portions of the ingot during initial heating. As the material is melted, liquid is levitated until it comes in contact with the upper portion of the ingot. After thermal equilibrium is reached, the induced power is controlled to establish a stable liquid zone. The shape of the molten zone and dimensional control of the freezing solid–liquid interface can be maintained by moving the top portion of the ingot relative the bottom (stretch/squeeze), while at the same time the lower solid portion of the ingot is rotated to maintain a smooth solid–liquid interface. The whole assembly is moved through the heating and shaping induction field. The current design of the solidification laboratory allows automated process control of the levitation zone refiner and the solidification process. Additional details on the facility and equipment operation have been presented elsewhere.[12,13]

Typically, two processing passes are necessary to produce clean bulk metallurgical samples from the NiAl–Cr precursor ingots. During the first pass, oxide inclusions and other impurities migrate to the surface of the liquid zone and are deposited on the surface of the ingot. The surface of the ingot and associated impurities are then removed by machining, and the ingot is processed a second time. Automated control of the solidification process is performed by real-time image analysis of the molten zone. During the first pass,
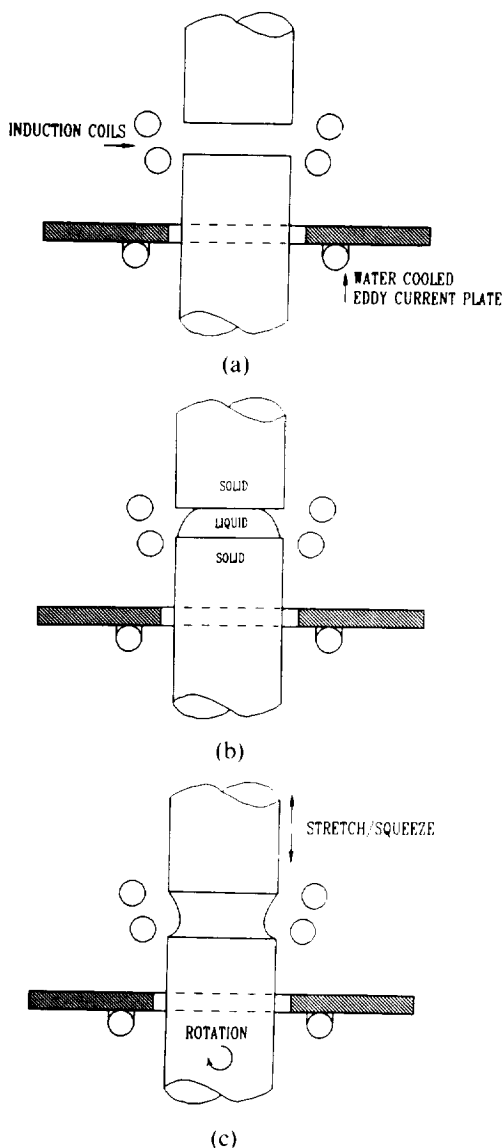
Fig. 1. Formation of an electromagnetically constrained liquid zone during containerless processing: (a) position at start; (b) zone partially established, liquid partially leviated; (c) zone established.

oxide particles (with a higher spectral emissivity) make the image analysis difficult and prevent tight dimensional control of the freezing solid–liquid interface. After a cleaning pass is made, automated control is possible and good dimensional control can be maintained, as demonstrated by the NiAl–33·4Cr–0·6Mo ingot shown in Fig. 2.
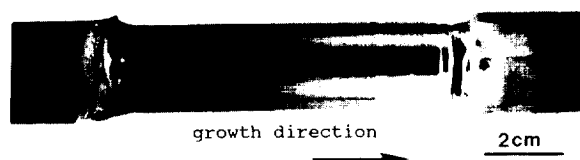

growth direction   2cm

Fig. 2. As-processed NiAl–33·4Cr–0·6Mo ingot (two passes).

Table 1. Composition and processing conditions for NiAl–Cr alloys

Composition (at.%)	Growth velocity (mm/h)	Rotational velocity (rpm)	Number of passes
NiAl–34CR	25	140	2
NiAl–34Cr–0·1Zr	13	100	3
NiAl–33·4Cr–0·6Mo	19	100	2
NiAl–33Cr–1·0Mo	13	40	2
NiAl–31Cr–3Mo	19	35	2[a]
NiAl–28Cr–6Mo	19	150	2
NiAl–34Cr	Induction melted and cast		

[a]Cooling jacket used for increased thermal gradient.

To compare the behavior of a directionally solidified eutectic to conventionally cast material, a NiAl–34Cr alloy was induction melted and cast into bars, using an alumina shell mold. Fracture toughness samples were then machined from the conventionally cast ingot.

In addition, the thermal gradient through the liquid/solid interface was increased during one directional solidification run in an attempt to produce a better aligned microstructure. To produce the steeper thermal gradient, a cooling jacket was mounted below the eddy current plate (see Fig. 1) in the levitation zone refiner. The cooling jacket consisted of four water cooled rings (40 mm diameter) that supported a series of thin copper strips that made mechanical contact with the ingot. A NiAl–31Cr–3Mo ingot was directionally solidified using this cooling jacket. The compositions and processing conditions for all the materials used in this study are listed in Table 1.

3 EXPERIMENTAL PROCEDURES

3.1 Compression testing

Cylindrical compression specimens, 5 mm diameter by 10 mm length, with the compression axis parallel to the growth direction, were electrical discharge machined from selected ingots. The elevated temperature mechanical behavior of these alloys was then determined. If promising strengths were measured at 1300 K, further testing at 1200 and 1400 K was performed. Compressive properties were generated under both constant velocity conditions in a screw driven universal machine and under constant load conditions in lever-arm creep machines. In general, constant velocity experiments were used to determine behavior at the higher strain rates ($> 10^{-7}$ s), while constant load testing was employed for lower rates. Overlapping

stress–strain rate data from the two techniques indicated excellent correlation between constant load and constant rate tests. All testing was performed in air as a secondary check for environmental resistance under load.

3.2 Flexure testing

Four-point bend specimens with nominal dimensions of 6·5 mm × 4·5 mm × 40 mm were electrical discharge machined from the directionally solidified ingots. A 2·0 mm × 0·35 mm notch was cut into each specimen with a slow speed diamond impregnated saw. A fatigue crack was not initiated at the notch tip prior to testing. The length of each bend specimen was oriented parallel to the growth direction of the solidified ingot with the notch perpendicular to the growth direction. Bend tests were performed on a screw driven test frame, using a displacement rate of $8·5 \times 10^{3}$ mm/s. The four-point loading geometry consisted of a 30 mm outer span and a 15 mm inner span. Fracture toughness values were calculated using the K calibration for pure bending.[14]

Most of the bend specimens were tested in the as-processed condition. However, heat treatments were performed on a number of specimens to investigate the effect of long term thermal exposure on properties. Selected bend specimens were encapsulated in silica tubing and back filled with argon to produce 1 atm pressure at 1300 K. The samples were then heat treated at 1300 K for 1·8 × 10^{6} s (500 h) and air cooled. After heat treatment, the samples were notched and the room temperature fracture toughness was determined by performing four-point bend tests as described previously.

3.3 Metallography

Light optical microscopy was used to characterize the general morphology and the degree of alignment for the eutectic microstructures after directional solidification. Longitudinal and transverse sections taken from each directionally solidified ingot were metallographically prepared and etched with a solution of 5% HF–5% HNO_3–90% H_2O by volume.

Scanning electron microscopy (SEM) was used to characterize the fracture surfaces of the bend specimens. Secondary electron imaging was used to examine the topology of the fracture surfaces. However, backscattered electron imaging was often used in conjunction with secondary electron

imaging to enhance phase contrast. The sides of the bend specimens were also studied under backscattered electron conditions near the notch to characterize the microcracking adjacent to the fracture surface. In all cases a beam voltage of 20 keV was used.

Transmission electron microscopy (TEM) was used to characterize further the microstructure and to study the dislocation structure. Thin slices were taken from broken bend specimens, both parallel and perpendicular to the growth direction, using a low speed diamond saw. The TEM specimens were taken as close to the fracture surface as possible. Thinning was performed by grinding and dimple grinding followed by twin-jet electropolishing in a solution of 5 %vol. perchloric acid, 95 %vol acetic acid at 40 V and 300 K.

4 MICROSTRUCTURES

4.1 Optimal microscopy

Typical microstructures of the conventionally cast eutectic and the directionally solidified ingots are shown in Figs 3 and 4. The conventionally cast NiAl–34Cr alloy was characterized by a cellular structure with a coarse eutectic spacing near the cell boundaries (Fig. 3(a) and (b)). A fibrous reinforcement morphology was observed for the directionally solidified NiAl–34Cr and NiAl–33·4Cr–0·6Mo eutectic alloys (Fig. 3(c) and (d) and (e) and (f) respectively). Microstructures from these alloys are characterized by an array of discontinuous chromium fibers that are aligned parallel with the growth direction and embedded within a single crystal NiAl matrix. Also evident in Fig. 3(c)–(f) are growth faults that lie perpendicular to the growth direction.

Molybdenum additions greater than 0·6 at.% tended to produce a lamellar reinforcement morphology, as seen in Fig. 4. The microstructures of these NiAl–(Cr,Mo) alloys consisted of eutectic cells composed of chromium plates within a NiAl matrix. Good alignment of the reinforcing phase was produced in the NiAl–31Cr–3Mo alloy (Fig. 4(c) and (d)). The NiAl–33Cr–1Mo and the NiAl–28Cr–6Mo alloys had similar microstructures, but exhibited poor alignment of the refractory metal phase (Fig. 4(a) and (b) and (e) and (f)), respectively. Hence, the good alignment of the NiAl–31Cr–3Mo microstructure was probably a result of the increased thermal gradient provided by the cooling jacket during processing.
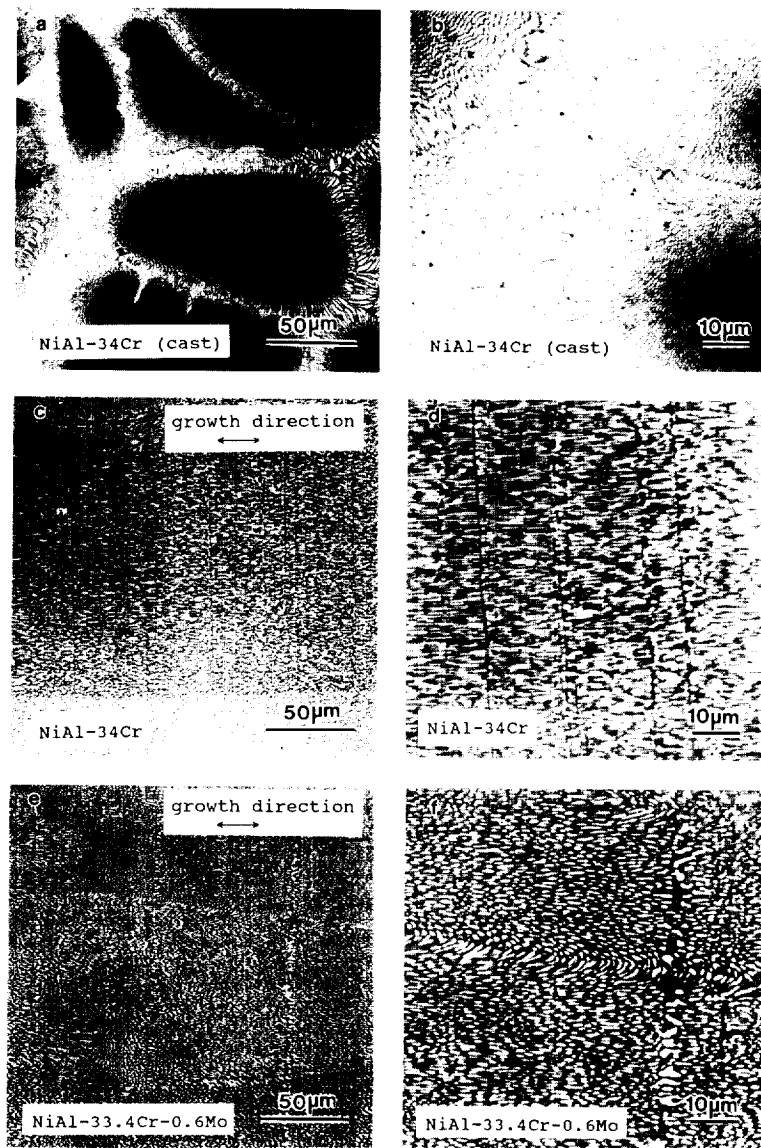
Fig. 3. Light optical photomicrographs taken from longitudinal sections of (a) and (b) conventionally cast, and (c)–(f) directionally solidified eutectics having a fibrous second-phase morphology.

A number of growth defects that consist of parallel bands running perpendicular to the growth direction exist in the directional solidified microstructures. These bands are characterized by a change in eutectic spacing or a complete interruption of the eutectic microstructure. The origin of these banding growth defects is presently unknown and does not appear to correlate with the different automated control schemes used.

Some important differences between the banding morphology exist between fibrous and lamellar eutectic microstructures. When the NiAl–Cr alloys have a fibrous morphology, the banding defects can consist of uninterrupted layers of NiAl (Fig. 3(d)). The unreinforced NiAl phase within the banded region is expected to have extremely dele-

terious effects on the mechanical properties of the eutectic during tensile loading. In contrast, the density of banding defects in the lamellar microstructures is much less (Fig. 4). For the lamellar reinforced alloys, the banding defects are the result of different eutectic spacings but still contain the reinforcing metal phase (Fig. 4(a)). Thus, the effects of banding in the lamellar microstructures are expected to be less severe than in the fibrous microstructures.

4.2 TEM results

Consistent with previous observations of the NiAl–Cr eutectic,[7] TEM results confirmed a cube-on-cube crystallographic relationship between the
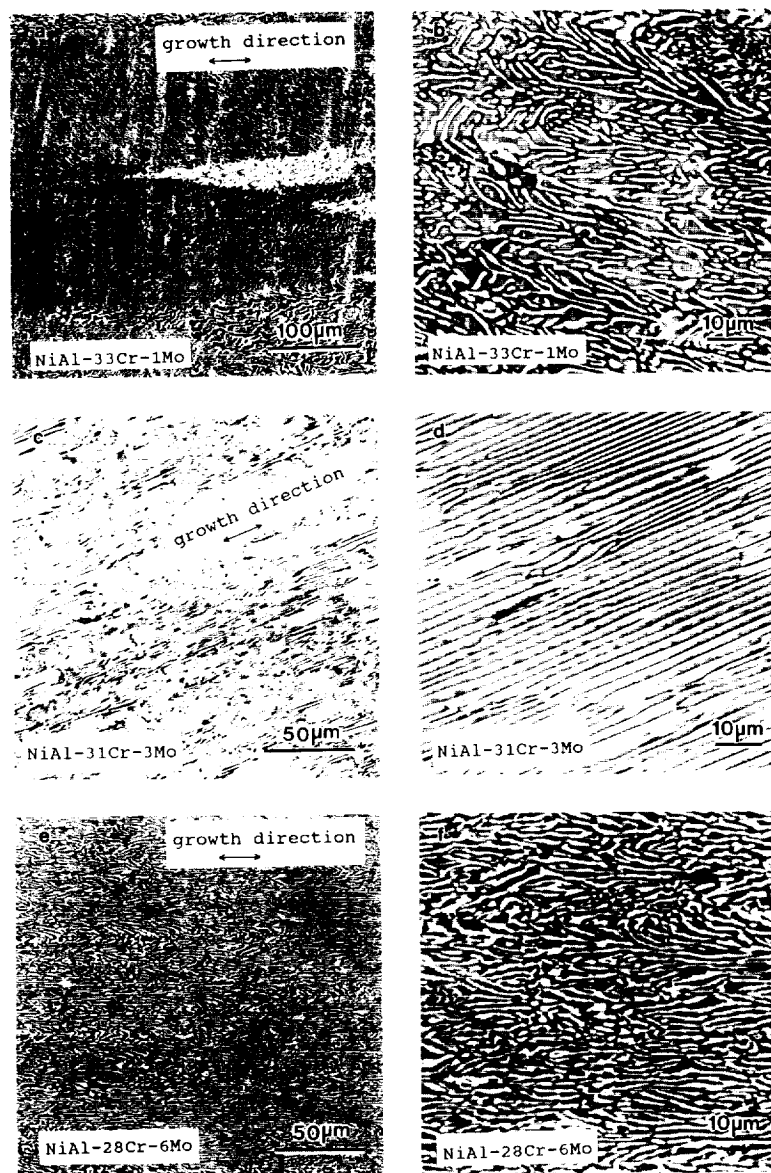
Fig. 4. Light optical photomicrographs taken from longitudinal sections of directionally solidified NiAl-(Cr,Mo) eutectics having a lamellar second-phase morphology.

NiAl matrix and the chromium phase as determined from selected area diffraction patterns. Also, a <100> growth direction was determined for the NiAl–34Cr eutectic while a <111> growth direction was found for the NiAl–28Cr–6Mo ingot with the lamellar morphology.

A semicoherent interface exists between the chromium-rich metal phase and the NiAl matrix due to the small lattice mismatch between the two phases.[8,9] The lattice mismatch is accommodated by a network of interface dislocations as shown in Fig. 5. The dislocation spacing along the interface is much smaller for the NiAl–28Cr–6Mo alloy than for the NiAl–34Cr eutectic. This is due to the greater mismatch in lattice parameter between NiAl and (Cr,Mo) than for NiAl and Cr.[9]

In addition, arrays of fine precipitates were observed in the chromium-rich metal phase of the NiAl–28Cr–6Mo alloy (Fig. 6). After heat treating at 1300 K, these precipitates coarsened and were determined to be NiAl.[15] Precipitates of this nature were not observed in the chromium phase of the NiAl–34Cr eutectic before or after heat treatment.

5 ELEVATED TEMPERATURE STRENGTH

Two directionally solidified ingots were selected for measurement of elevated temperature strength: the NiAl–34Cr–0·1Zr alloy with a fibrous eutectic morphology and the NiAl–28Cr–6Mo alloy consisting of a lamellar microstructure. Elevated
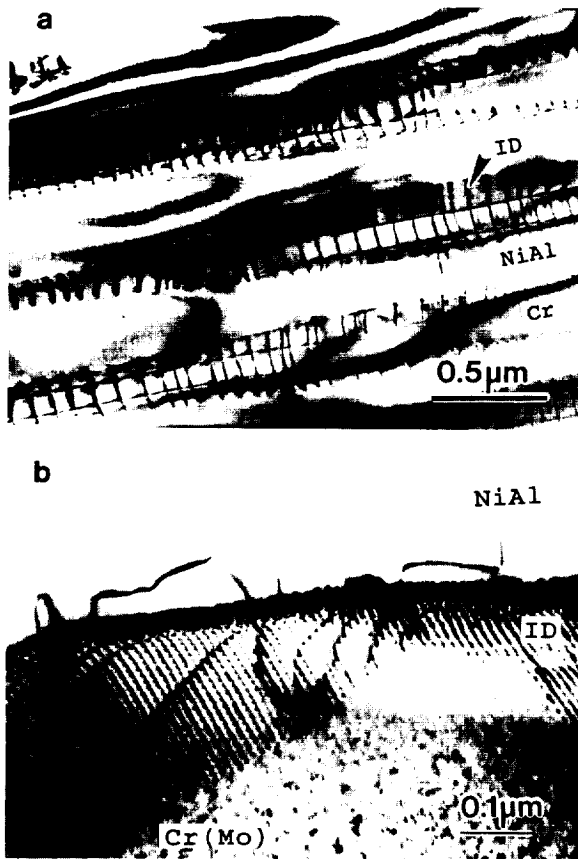
Fig. 5. TEM photomicrographs of the interface dislocations (marked 'ID') between the NiAl matrix and Cr-rich metal phase for (a) NiAl-34Cr eutectic and (b) NiAl 28Cr-6Mo eutectic.

temperature properties were determined in compression at 1300 K for both alloys. The NiAl–28Cr–6Mo alloys showed promising creep strength so additional testing was performed at 1200 and 1400 K. Zirconium was added to the NiAl–34Cr eutectic in an attempt to enhance the oxidation resistance of this alloy. Trace additions
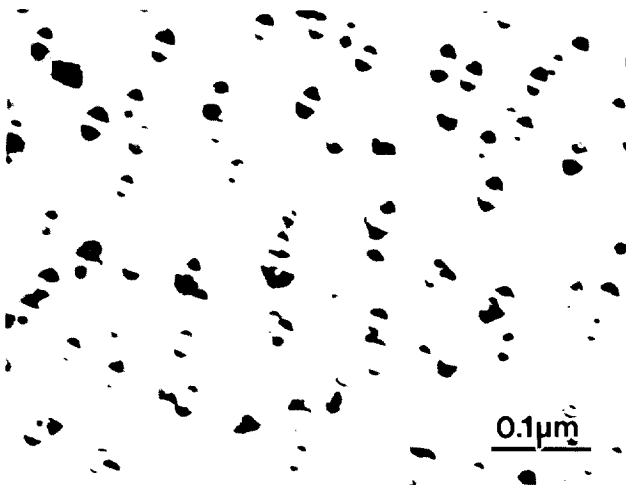

Fig. 6. TEM photomicrograph showing fine NiAl precipitates within the Cr-rich lamella from an as-processed NiAl–28Cr 6Mo eutectic.

of zirconium are known to improve greatly the cyclic oxidation resistance of NiAl.[16] Compression tests were not performed on the well-aligned NiAl–31Cr–3Mo alloy due to a lack of material.

The flow stress and strain rate, $\dot{\epsilon}$, data were fitted to a power law or a temperature compensated-power law equation:

$$\dot{\epsilon} = A\sigma^n$$

or

$$\dot{\epsilon} = B\sigma^n\exp(-Q/RT)$$

where A and B are constants, σ is the applied true stress (MPa), Q is the activation energy for deformation (kJ/mol), T is the absolute temperature, R is the gas constant, and n is the stress exponent. The creep characteristics for the NiAl–34Cr and NiAl–28Cr–6Mo alloys are compared to that of single crystal NiAl in Table 2.

In Fig. 7 the 1300 K compressive creep behavior of the NiAl–Cr and NiAl–(Cr,Mo) alloys are compared to single crystal binary NiAl (Whittenberger, J. D. and Noebe, R. D., 1991, unpublished) and a nickel-based single crystal superalloy.[17] The creep characteristics, stress exponent and activation energy for deformation, are similar for the eutectic alloys and binary NiAl. However, the NiAl–Cr and NiAl–(Cr,Mo) alloys have significantly higher strengths compared to binary NiAl. Of the two eutectic alloys, the lamellar NiAl–(Cr,Mo) alloy displays a slightly greater strength over the strain rates tested. While the NiAl–Cr and NiAl–(Cr,Mo) alloys are much stronger then binary NiAl, they are still weaker than a single crystal nickel-based superalloy. The elevated temperature strength of the NiAl–28Cr–6Mo ingot over the temperature range 1200–1400 K is shown in Fig. 8. Except for the fastest strain rates at 1200 K where power-law breakdown behavior has occurred, the NiAl–28Cr–6Mo eutectic exhibits a very consistent power law behavior over the strain rates and temperatures investigated.

Table 2. Representative creep behavior of NiAl–Cr eutectic alloys compared to binary NiAl

Alloy	Representative creep behavior
NiAl [001] (Ni–50Al)	1100–1300 K: $\dot{\epsilon} = (1.48 \times 10^3)\,\sigma^{6.3}\exp(-439.3/RT)^a$
NiAl–Cr (Ni–33Al–34Cr–0.1Zr)	1300 K: $\dot{\epsilon} = (3.52 \times 10^{-23})\,\sigma^{7.69}$
NiAl (Cr,Mo) (Ni–33Al–28Cr–6Mo)	1200–1400 K: $\dot{\epsilon} = (1.99 \times 10^{-2})\,\sigma^{6.38}\exp(-456.6/RT)$

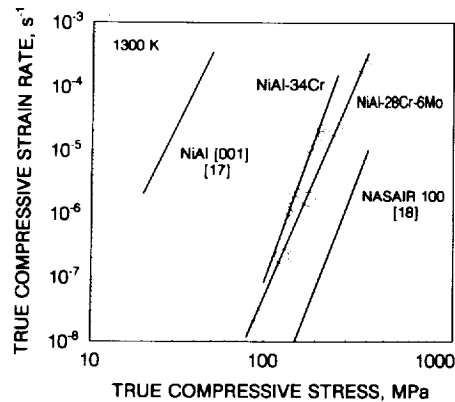[a]Whittenberger, J.D. and Noebe, R. D., unpublished data, 1991.

Fig. 7. 1300 K compressive flow stress strain rate behavior for the NiAl–34Cr and NiAl–28Cr-6Mo eutectics compared to NiAl and a single crystal superalloy.

Fig. 8. Compressive flow stress strain rate behavior for the NiAl–28Cr–6Mo eutectic as a function of temperature.

Generally, the strength of a directionally solidified eutectic is controlled by the strength of the second phase. Since the refractory metal phase in the NiAl–28Cr–6Mo eutectic is precipitation hardened by fine NiAl precipitates, this material would be expected to have better strength than the simple ternary NiAl–Cr alloy. In addition, the greater strength of the NiAl–28Cr–6Mo may be due to strengthening by the dislocation networks at the semicoherent interface between the chromium-rich phase and NiAl. Cline et al.[9] suggested that the strengthening should be proportional to the lattice mismatch and hence the dislocation density along the interface. From their data, the mismatch for the NiAl–28Cr–6Mo eutectic should be greater than for the NiAl–34Cr eutectic for all temperatures up to the melting point. However, the actual difference in strength between the two eutectic alloys, especially at lower strain rates, is not as large as the previous arguments may suggest. While the network of interface dislocations is immobile and constrained to lie along the interface, it may act as a source or sink for other
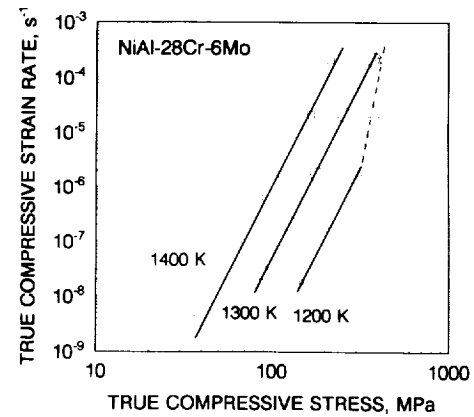
dislocations. Therefore, a larger lattice mismatch may not provide strengthening at low deformation rates such as those in the creep regime.

6 ROOM TEMPERATURE TOUGHNESS

The room temperature fracture toughness data for the eutectic alloys are listed in Table 3. The fracture toughness of the directionally solidified NiAl–Cr and the NiAl–(Cr,Mo) eutectics are much higher than that of binary NiAl. The directionally solidified eutectic alloys have a fracture toughness of 20 to 22 $MPa\sqrt{m}$ as opposed to 6 $MPa\sqrt{m}$[18] for polycrystalline NiAl or even 11 $MPa\sqrt{m}$[11] for zone-refined single crystal NiAl. However, the improvement in toughness is only maintained for aligned, directionally solidified microstructures since the conventionally cast NiAl–34Cr alloy had a fracture toughness of only 6 $MPa\sqrt{m}$.

For the directionally solidified materials, the addition of molybdenum to the NiAl–Cr eutectic,

Table 3. Room temperature fracture toughness of directionally solidified NiAl–(Cr, Mo) and induction melted and conventionally cast NiAl–34Cr eutectic alloys

Alloy	K_1 ($MPa\sqrt{m}$)	Alloy	K_1 ($MPa\sqrt{m}$)
NiAl–34Cr–0·1Zr	19·2	NiAl–31·4Cr–0·6Mo	22·2
		NiAl–31·4Cr–0·6Mo	16·7
NiAl–34Cr	20·4	NiAl–31·4Cr–0·6Mo	19·6
NiAl–34Cr	18·5		
NiAl–34Cr	21·5	NiAl–31Cr–3Mo	21·1
NiAl–34Cr	20·7	NiAl–31Cr–3Mo	22·2
NiAl–34Cr	20·8	NiAl–31Cr–3Mo	22·0
NiAl–34Cr (cast)	6·0	NiAl–28Cr–6Mo	22·6
NiAl–34Cr (cast)	5·8	NiAl–28Cr–6Mo	24·1
NiAl–34Cr (cast)	5·6	NiAl–38Cr–6Mo	17·5
NiAl–34Cr (cast)	5·6	NiAl–28Cr–6Mo	22·2

Table 4. Room temperature fracture toughness of directionally solidified alloys heat treated at 1300 K for 1·8 × 10⁶ s (500 h) and air cooled

Alloy	K_1 (MPa√m)
NiAl–34Cr	21·8
NiAl–34Cr	20·4
NiAl–34Cr	21·7
NiAl–31Cr–3Mo	19·8
NiAl–31Cr–3Mo	21·3
NiAl–28Cr–6Mo	19·6

while not having a significant effect on the measured fracture toughness, did have other advantages. For a number of the NiAl–34Cr bend specimens, fracture did not initiate at the notch, invalidating the test. Instead fracture occurred at the banded growth defects described previously. In contrast, fracture initiated at the notch for all the NiAl–(Cr,Mo) alloys since any growth faults in these alloys were not composed of eutectic free zones. Moreover, two of the NiAl–31Cr–3Mo specimens did not break into two separate halves after fracture initiation, but instead exhibited a strong crack arrest behavior. These specimens could be handled quite easily without further propagation of the crack. The crack arrest behavior displayed by the NiAl–31Cr–3Mo bend specimens is due to the well-aligned microstructure. The NiAl–28Cr–6Mo specimens, having a cellular microstructure, did not display this behavior.

Heat treating the bend specimens at 1300 K did not change the fracture toughness significantly. The toughness of both the NiAl–Cr and NiAl–(Cr,Mo) alloys after heat treatment were similar to those in the as-processed condition (Table 4). Consistent with the fracture toughness values, no major changes in eutectic morphology were observed after heat treatment. These results indicate that the eutectic morphologies are stable under isothermal conditions.

7 ROOM TEMPERATURE FRACTURE CHARACTERISTICS

In general, ductile phase toughening is an effective method for increasing the toughness of NiAl.[2] Heredia et al.[19] recently reviewed the different toughening mechanisms they observed in the NiAl–refractory metal eutectics. The improved fracture toughness and the fracture characteristics of NiAl-based eutectics originate from both

initiation toughness and subsequent crack growth toughness processes. These toughening mechanisms include crack trapping, crack renucleation and crack bridging.

The initiation toughness depends upon the ductile phase morphology. For a fibrous microstructure, such as the NiAl–Cr eutectic, a crack trapping mechanism controls the initiation toughness. The crack front in this process is trapped (or hindered) by tough second-phase particles whose fracture toughness value exceeds the local stress intensity.[20,21] For a lamellar microstructure, such as the NiAl–(Cr,Mo) eutectic, the crack front cannot surround the tough second-phase particles and must renucleate in the adjacent material.[19,22,23] With both toughening mechanisms, the crack may also be blunted or deflected by the ductile phase.

Once a crack has initiated, unbroken second-phase fibers or lamellae may lag behind the crack front. The plastic work expended upon stretching these second-phase particles during crack propagation provides a resistance to crack growth and is referred to as crack bridging.[24,25] The amount of toughening provided by crack bridging depends upon the volume fraction and flow characteristics of the second phase and the amount of debonding present at the ductile phase/matrix interface. Partial debonding at the interface enhances the toughening effect of the ductile phase.[24]

Examination of microcracking near the notched region of broken bend specimens may offer some insight into the operative fracture mechanisms. The fracture behavior of the NiAl–34Cr and the NiAl–31Cr–3Mo bend specimens is shown in Fig. 9. These photomicrographs were taken along the side of the bend specimen perpendicular to the fracture surface. The volume fraction of the chromium-rich metal phase is essentially the same in both microstructures. However, the morphology and growth orientation are different. For the NiAl–34Cr microstructure, the angle between the crack and the <100> growth direction is nominally 45°. This observation is consistent with a <110> type cleavage plane for NiAl.[26]

Crack bridging by the refractory metal phase is evident in both microstructures. In addition, crack renucleation and crack deflection mechanisms are visible in the lamellar microstructure (Fig. 9(b)). Additional examples of crack bridging for the two different eutectic morphologies are shown in Fig. 10. Partial debonding along the phase boundary and necking of the metal phase are visible. In all the specimens tested, a crack bridging mechanism was observed. Therefore, the amount of toughening

Fig. 9. SEM backscattered electron photomicrographs of microcracking in (a) NiAl 34Cr bend specimen and (b) NiAl 31Cr 3Mo bend specimen.

Fig. 10. SEM backscattered electron photomicrographs of crack bridging in (a) NiAl 34Cr eutectic and (b) NiAl 28Cr 6Mo eutectic.

provided by a crack bridging mechanism was estimated to determine the percentage of the toughness increase due to this particular mechanism.

7.1 Crack bridging

The increase in fracture energy, ΔG, due to a crack bridging mechanism has been described by Mataga[24] and Flinn et al.[26] and can be written as

$$\Delta G = G - G_m = f \int_0^{u^*} \sigma du - f G_m$$

where G_m is the fracture energy for the matrix, f is the volume fraction of the ductile phase, and u^* is the crack opening displacement needed to rupture the ductile phase.
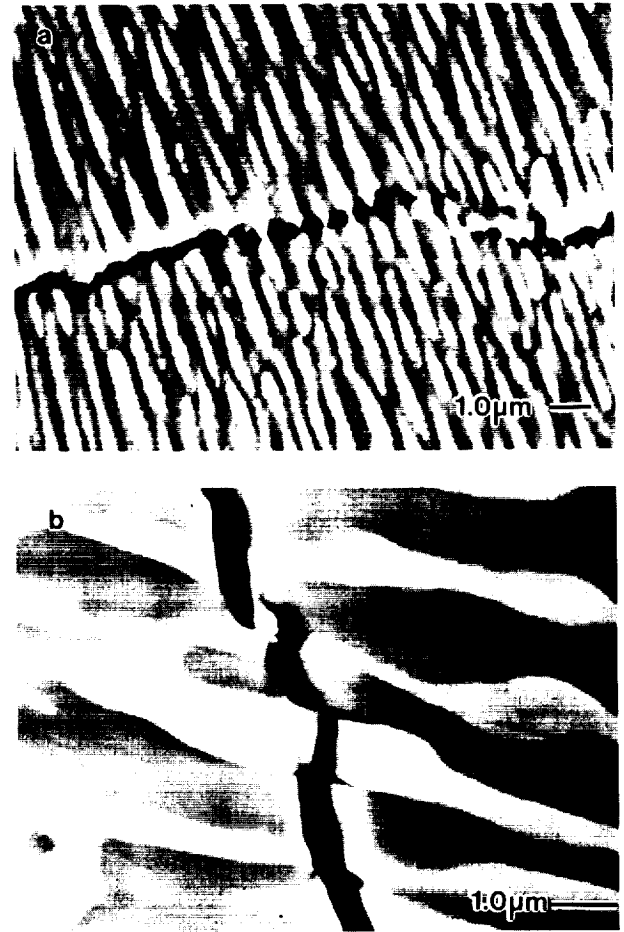Rearranging:

$$G = (1-f) G_m + f \int_0^{u^*} \sigma du$$

or

$$G = G_m (1-f) + f \sigma_o a_o \chi$$

where σ_0 is the yield stress of the ductile phase, a_0 is the radius of the ductile phase, and χ is the work of the rupture parameter,[25] which depends on the flow characteristics of the ductile phase and the amount of plastic constraint present. The amount of plastic constraint is controlled by the interfacial strength and the amount of decohesion between the ductile phase and the matrix. The work of the rupture parameter, χ, is approximately the ratio between the work needed to fracture the constrained ductile phase to that of the unconstrained case. Experimental studies of lead wires or sheets constrained within a glass matrix have shown that χ can vary from 1 (unconstrained) to about 6 when partial decohesion is present.[27,28] Converting the energy for fracture to the stress intensity factor in plane strain by $K^2(1-\nu^2) = GE$, where ν is Poisson's ratio, and E is the elastic modulus gives[29]

$$K_{\text{Ic}} = \sqrt{\frac{K_{\text{m}}^2(1-\nu_{\text{m}}^2)\,(1-f)E_{\text{c}}}{E_{\text{m}}(1-\nu_{\text{c}}^2)} + \frac{fE_{\text{c}}\sigma_{\text{o}}a_{\text{o}}\chi}{(1-\nu_{\text{c}}^2)}} \quad (1)$$

(subscripts: m = matrix, c = composite)

Ravichandran used such a model to predict the fracture toughness of a wide range of ductile phase composites with good results, with an assumption that $\chi = 4$.[29]

To apply this model to the NiAl–Cr and NiAl–(Cr,Mo) eutectics, the elastic and plastic properties of the composite and constituent phases must be estimated. The elastic properties of NiAl and chromium for <100> and <111> oriented crystals[30,31] are listed in Table 5. The rule of mixtures was used to estimate the elastic properties of the eutectic alloys. The yield strength of the eutectic and the constituent phases was estimated from compressive yield strength data[5] and from microhardness measurements. These data are listed in Table 6. Due to the fineness of the eutectic micro-structure, the microhardness values for the constituent

Table 5. Elastic modulus for <100> and <111> oriented crystals of NiAl and Cr

Material	Orientation	E(GPa)	Poisson's ratio
NiAl	[100]	95·9	0·404
Cr	[100]	325	0·159
NiAl	[111]	277	0·222
Cr	[111]	248	0·239
Rule of mixtures (vol. fract. Cr = 34%)			
NiAl–34Cr	[100]	174	0·321
NiAl–Cr,Mo	[111]	263	0·228

Table 6. Vickers microhardness and estimated or measured strength data for NiAl–Cr and various NiAl–Cr alloys

Material	Vickers microhardness (kg/mm²)	Yield stress (MPa)
Arc-melted NiAl-Cr alloys heat treated at 1100 K for 9000 s (2·5 h) and furnace cooled		
NiAl (high purity)	276	—
NiAl,Cr (NiAl–10Cr)	431	560[a,33]
Eutectic (NiAl–34Cr)	481	700[a]
Cr,NiAl (NiAl–90Cr)	589	990[b]
Cr (high purity)	189	—
Compressive yield strength values for [100] oriented crystals of a directionally solidified NiAl-34Cr eutectic and a NiAl single crystal		
NiAl [100]	··	1400[5]
NiAl–34Cr [100]	370	1240[5]
Cr-rich solid solution	··	930[b]

[a]Estimated from the hardness versus yield strength data in Ref. 3 after scaling hardness values relative to the hardness of the directionally solidified ingot (370/481).
[b]Rule of mixtures using a volume fraction of chromium = 34%.

phases were determined from arc-melted ingots.[32]

Substituting the data from Tables 5 and 6 into the crack bridging model along with the following data: $f = 0.34$ for the volume fraction of chromium, $a_0 = 0.3$ μm from SEM photomicrographs, $K_{\text{IC}} = 11$ MPa√m for NiAl having <100> crystal orientation,[11] $K_{\text{IC}} = 9$ MPa√m for NiAl having a non-<100> crystal orientation,[34] and $\chi = 4$ (first approximation), gives the following results.

For the NiAl-Cr eutectic with a <100> growth direction:

$$K_{\text{IC}} = \sqrt{1 \cdot 12 K_{\text{m}}^2 + 19 \cdot 6\chi} \quad \text{or} \quad K_{\text{IC}} = 15 \quad (2)$$

For the NiAl–(Cr,Mo) eutectic with a <111> growth direction:

$$K_{\text{IC}} = \sqrt{0 \cdot 628 K_{\text{m}}^2 + 28 \cdot 1\chi} \quad \text{or} \quad K_{\text{IC}} = 13 \quad (3)$$

These values underestimate the measured values, indicating that crack bridging is not the only toughening mechanism in these microstructures.

7.2 Crack initiation toughness

Given the increase in fracture toughness due to crack bridging alone, it is evident that other toughening mechanisms must also be responsible for the measured toughness of the NiAl–Cr and NiAl–(Cr,Mo) alloys. The initiation toughness of these alloys can be described by a crack trapping mechanism for fibrous microstructures or by a crack renucleation mechanism for lamellar microstructures. Evidence for each of these mechanisms can be found in the fracture surfaces of these alloys, as demonstrated in Fig. 11. A crack trapping mechanism is clearly visible for the fibrous NiAl–34Cr eutectic (Fig. 11(a)). Consistent with a crack renucleation event, the lamellar morphology of the metal phase is visible on the fracture surface of the NiAl–31Cr–3Mo alloy (Fig. 11(b)). Plastic stretching of the chromium-rich metal phase is also evident for the lamellar NiAl–31Cr–3Mo eutectic.

Heredia *et al.*[19] measured the initiation toughness of a lamellar NiAl–(Cr,Mo) eutectic at 17 MPa√m. Using this value instead of 9 MPa√m for the initiation toughness, a value of $\chi = 11$ in eqn (3) is still needed for the work of the rupture parameter to account for the measured toughness of the NiAl–(Cr,Mo) specimens. Since extensive plastic deformation of the chromium-rich metal phase is not observed, such a high value for the work of the rupture parameter is unreasonable.
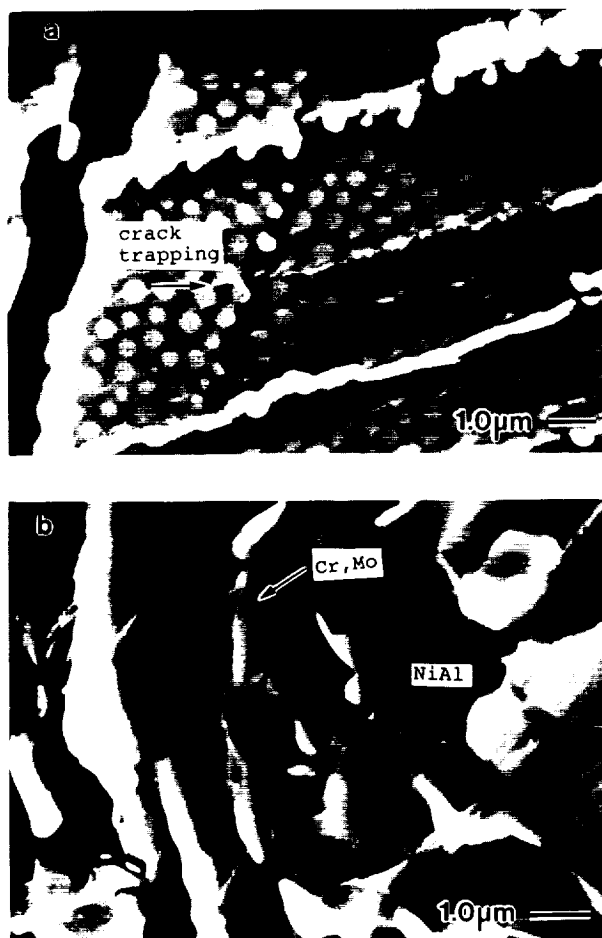
Fig. 11. SEM photomicrographs showing the fracture surface (transverse to the growth direction) from (a) NiAl 34Cr eutectic and (b) NiAl 31Cr 3Mo eutectic.

Hence, still other toughening mechanisms must be operative, at least in the NiAl–(Cr,Mo) alloys.

For the fibrous NiAl Cr eutectic, using an initiation toughness of 17 MPa$\sqrt{m}$ with $\chi = 4$ in eqn (2) gives a fracture toughness of 20 MPa$\sqrt{m}$, which is much closer to the measured values. An estimate of $\chi = 4$ is not unreasonable, based on the plastic deformation of the chromium fibers bridging the crack path (Figs 9 and 10). While the chromium fibers do not neck to a point (Fig. 11) as in the NiAl Mo eutectic,[5,19, 34] any plastic deformation of the chromium-rich phase is somewhat surprising given the brittle nature of chromium alloys. For example, the arc-melted NiAl–90Cr ingot (Table 6) was found to be extremely brittle. However, even with practically no plastic deformation, a value nearing $\chi = 2$ would be expected due to the plastic constraint of the chromium fibers. For plane strain conditions, the average value of the effective yield stress is larger than the uniaxial yield stress by a calculated factor of 1·68 with experimentally determined values

ranging between 1·5 and 2.[35] The fact that some deformation of the chromium-rich phase is observed suggests that the work of the rupture parameter should be greater than $\chi = 2$, which demonstrates the potent toughening effect from a crack bridging mechanism in these alloys.

7.3 Linkage of microcracks

A toughening mechanism similar to that of shear ligament toughening, described by Chan[36] for two-phase TiAl alloys, is also observed in the NiAl–Cr and NiAl–(Cr,Mo) alloys. Crack deflection and renucleation caused by the tough second-phase reinforcement may result in a series of microcracks. The material between the microcracks should fracture by shear as the microcracks connect with the main crack. Linkage of these microcracks with the main crack may then provide further resistance to crack growth.

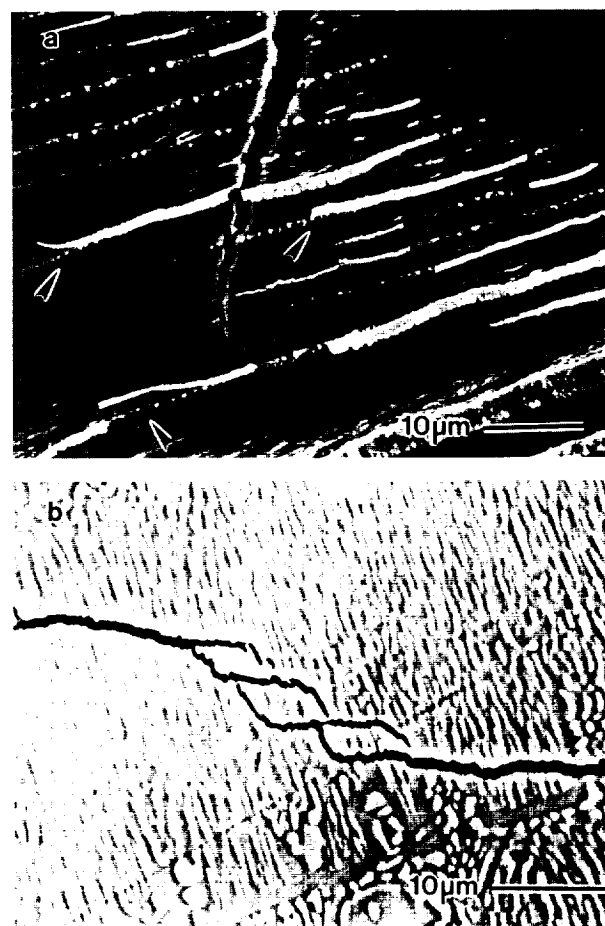The fracture surface of a NiAl–34Cr bend specimen is shown in Fig. 12. Characteristic of this type

Fig. 12. Linkage of microcracks by shear deformation in a NiAl-34Cr eutectic showing (a) 'strips' of material displaced from the fracture surface by a shear strain (marked with arrows), and (b) microcracking along the side of the bend specimen.

Fig. 13. Linkage of microcracks by shear deformation in a NiAl–28C–6Mo eutectic showing (a) 'strips' of material displaced from the fracture surface by a shear strain (marked with arrows), and (b) microcracking along the side of the bend specimen.

of fracture mechanism, 'strips' of material, containing both the chromium rods and the NiAl matrix, have separated from the fracture surface due to the linkage of microcracks. Often these 'strips' have peeled away from the fracture surface and appear to be plastically deformed. As evident in Fig. 12(a), a shear strain has displaced the 'strips' of material normal to the fracture surface. Formation of these 'strips' can be visualized in Fig. 12(b), which shows the linkage of a series of microcracks in the NiAl–34Cr bend specimen. A similar mechanism is observed in the lamellar NiAl–(Cr,Mo) alloys, as shown in Fig. 13. While the amount of toughening due to this mechanism is not known, it was widely observed on the fracture surfaces of the directionally solidified bend specimens.

7.4 TEM observations

For material taken very near the fracture surface,

regions of localized deformation are evident by the strain contrast produced by slip band formation (Fig. 14). In all the specimens examined, the dislocation density found in the NiAl phase was much greater than that of the chromium-rich metal phase.[32] The low number of dislocations found in the chromium-rich metal phase is attributed to the greater yield strength of the chromium solid solution compared to the yield strength of non-<100> oriented crystals of NiAl (Table 6). However, plastic deformation of the metal phase by a crack bridging mechanism is clearly evident in Fig. 10. Hence, to account for the low dislocation density observed in the chromium phase, NiAl must deform and fracture before the yield strength of the chromium-rich phase is exceeded. The bridging chromium-rich phase then deforms in the crack wake. Specimens for TEM studies were taken below the fracture surface and thus away from the necked regions of the refractory metal phase.

Cotton *et al.*[37] have shown that the slip system in NiAl is not altered by chromium additions and is predominantly <100>{011} at room temperature. To see if the molybdenum additions had any affect on the slip behavior of the NiAl–Cr solid
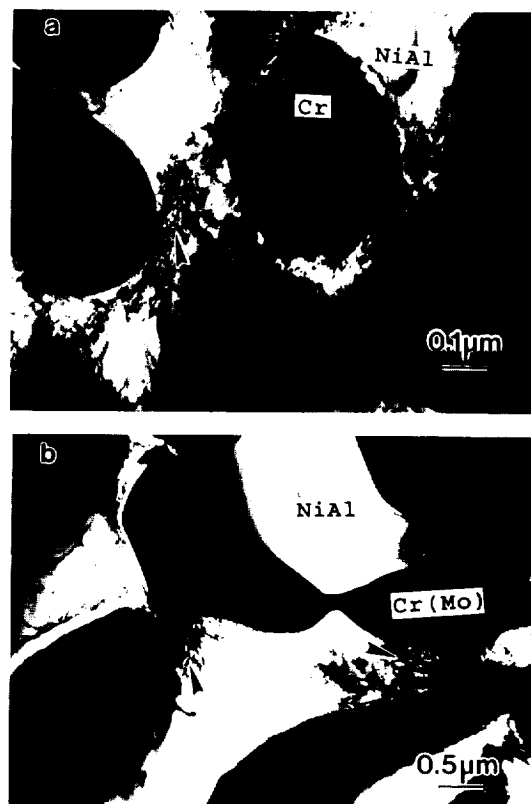

Fig. 14. TEM photomicrographs from samples taken very near the fracture surface showing slip band activity (marked with arrows) for (a) NiAl–34Cr eutectic and (b) NiAl–28Cr 6Mo eutectic.
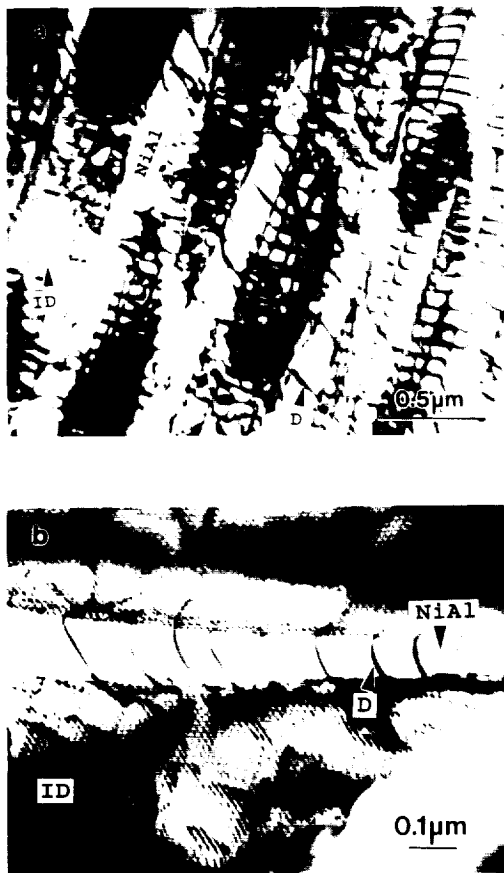
Fig. 15. TEM photomicrographs showing the dislocations (marked 'D') in NiAl that are generated and pinned by the interface dislocation network (marked 'ID') in (a) NiAl 34Cr eutectic and (b) NiAl 28Cr 6Mo eutectic.

solution, the Burgers vector was measured for dislocations observed near the fracture surface of a NiAl–28Cr–6Mo bend specimen.[15] Consistent with other NiAl alloys, only a <100> Burgers vector was measured for dislocations in the matrix phase.

As shown in Fig. 5, a dislocation network exists along the phase boundary between the eutectic phases. This network is constrained to lie along the metal/NiAl interface, strengthening the alloy. During deformation, new dislocations are generated from the interface network. These dislocations can then move into the NiAl matrix. However, due to the fineness of the eutectic microstructure, these dislocations are often pinned by neighboring interfaces (Fig. 15), providing further strengthening.

8 DISCUSSION

The most notable changes due to alloying with molybdenum were the changes in morphology and

growth direction. Both the room temperature fracture resistance and the elevated temperature strength of the NiAl–Cr eutectic were moderately improved by molybdenum additions. However, the change in growth direction from the 'hard' <100> orientation to a 'soft' <111> orientation cannot account for the increase in strength of the NiAl–(Cr,Mo) eutectic. In fact, the opposite effect would be expected.[38] Furthermore, the growth direction of the NiAl matrix has little effect on the measured fracture toughness of the eutectic, with similar values measured for both the <100> and <111> orientations. This result is somewhat surprising since the fracture toughness of single crystal NiAl differs by almost a factor of two for these orientations.[26]

Since the fracture toughness of the NiAl–Cr eutectic does not appear to be strongly dependent upon the toughness of NiAl, alloying approaches that strengthen the NiAl phase may not degrade the room temperature toughness of the eutectic. For example, hafnium additions may further increase the creep strength of NiAl–(Cr,Mo) alloys by strengthening the NiAl phase.

As a combination of properties, the elevated temperature strength and the room temperature toughness of the NiAl–(Cr,Mo) eutectic are good when compared to other NiAl–based eutectics, as shown in Fig. 16. Two classes of eutectics are compared in this figure, NiAl–Laves eutectics and NiAl refractory metal eutectics, all grown by the same containerless processing procedure described earlier. Promising creep strengths are found for the NiAl Laves alloys such as the NiAl–NiAlTa eutectic.[40] Unfortunately, these alloys are very brittle. Conversely, promising toughness values
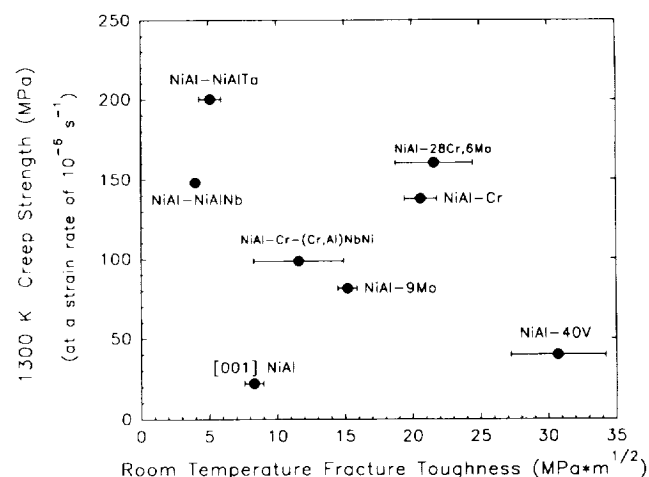

Fig. 16. Performance of NiAl-based directionally solidified eutectics compared to binary single crystal NiAl and a single crystal superalloy.

are found for the NiAl-refractory metal alloys such as the NiAl-V eutectic.[34] However, the oxidation resistance of this material is extremely poor. For the materials evaluated, the NiAl-(Cr,Mo) eutectic has the best combination of properties and hence has the most promise as a high temperature structural material.

9 CONCLUSIONS

Alloys based on the lamellar NiAl-(Cr,Mo) eutectic display a good combination of room temperature toughness and elevated temperature strength when compared to other NiAl-based eutectics. The NiAl-(Cr,Mo) eutectic shows promise as a high temperature material, but will require further property improvements to compete with nickel-based superalloys.

ACKNOWLEDGEMENTS

REFERENCES

1. Darolia, R., *JOM*, **43**(3) (1991), 44 9.
2. Noebe, R. D., Ritzert, F. J., Misra, A. & Gibala, R., Prospects for Ductility and Toughness Enhancement of NiAl by Ductile Phase Reinforcement, NASA TM-103796, 1991.
3. Walter, J. L. & Cline, H. E., *Met. Trans.*, **1** (1970) 1221 9.
4. Darolia, R., Larman, D. F., Field, R. D., Dobbs, J. R., Chan, K. M., Goldman, E. H. & Konitzer, D. G., In *Ordered Intermetallics—Physical Metallurgy and Mechanical Behavior*, eds C. T. Liu et. al. Kluwer Academic, Dordrecht, The Netherlands, 1991, pp. 679 98.
5. Johnson D. R., Joslin S. M., Oliver B. F., Noebe R. D. & Whittenberger J. D., In *Intermetallic Matrix Composites II*, eds. D. Miracle et. al., *MRS Sym. Proc.*, Vol. 273, Pittsburgh, PA, 1992, pp. 87 92.
6. Walter, J. L. & Cline, H. E., *Met Trans.*, **4** (1973) 33 8.
7. Cline, H. E. & Walter, J. L., *Met Trans.*, **1** (1970) 2907 17.
8. Walter, J. L., Cline, H. E. & Koch, E. F., *Trans. AIME*, **245** (1969) 2073–9.
9. Cline, H. E., Walter, J. L., Koch, E. F. & Osika, L. M., *Acta Met.*, **19** (1971) 405 14.
10. Merchant, S. M. & Notis, M. R., *Mater. Sci. and Eng.*, **66** (1984) 47 60.
11. Johnson, D. R., Joslin, S. M., Oliver, B. F., Noebe, R. D., & Whittenberger, J. D., In *1st Int. Conf. on Processing Materials for Properties*, eds H. Henein & T. Oki. TMS, Warrendale, PA, 1993, pp. 865 70.
12. Reviere, R. D., Oliver, B. F. & Bruns, D. D., *Mater and Manuf. Process*, **4**(10) (1989) 103 31.
13. Johnson, D. R., Joslin, S. M., Reviere, R. D., Oliver, B. F. & Noebe, R. D., In *Processing and Fabrication of Advanced Materials for High Temperature Applications II*, eds V. A. Ravi & T. S. Srivatsan. TMS, Warrendale, PA, 1993, 77 90.
14. Brown, W. F. & Srawley, J. E., In *Plane Strain Crack Toughness Testing of High Strength Metallic Materials*, ASTM Special Publication No. 410, ASTM, Philadelphia, PA (1966), pp. 13 14.
15. Chen, X. F., Johnson, D. R., Oliver, B. F. & Noebe, R. D., *Mat. Characterization* (to be submitted).
16. Nesbitt, J. A. & Barrett, C. A., In *Structural Intermetallics*, ed. R. Darolia et al. TMS, Warrendale, PA, 1993, pp. 601 10.
17. Nathal, M. V. & Ebert, L. J., *Metall. Trans. A*, **16A** (1985) 427 39.
18. Kumar, K. S., Mannan, S. K & Viswanadham, R. K., *Acta Metall. Mater.*, **40** (1992) 1201 22.
19. Heredia, F. E., He, M. Y., Lugas, G. E., Evans, A. G., Deve, H. E. & Konitzer, D., *Acta Metall. Mater.*, **41** (1993) 505 11.
20. Fares, N., *J. Appl. Mech.*, **56** (1989) 837 43.
21. Gao, H. & Rice, J., *J. Appl. Mech.*, **56** (1989) 828 36.
22. Chan, K. S., *JOM*, **44**(5) (1992) 30 8.
23. Chan, K. S., *Metal Trans. A*, **23A** (1992) 183 99.
24. Matage, P. A., *Acta Metall.* **37** (1989) 3349 59.
25. Flinn, B. D., Rühle, M. & Evens, A. G., *Acta Metall.*, **37** (1989) 3001 6.
26. Chang, K. M., Darolia, R. & Lipsitt, H. A., *Acta Metall. Mater.*, **40** (1992) 2727 37.
27. Ashby, M. F., Blunt, F. J. & Bannister, M., *Acta Metall.*, **37** (1989) 1847 57.
28. Bannister, M. & Ashby, M. F., *Acta Metall. Mater.*, **39** (1991) 2575 82.
29. Ravichandran, K. S., *Scripta Metall. Mater.*, **26** (1992) 1389-93.
30. Wasilewski, R. J., *Trans. AIME*, **236** (1966) 455 7.
31. *Smithells Metals References Book*, 6th edn. ed. E. A. Brandes. Butterworth, London, 1983, 15 5.
32. Chen, X. F., Johnson, D. R. & Oliver, B. F., *Scripta Metall. Mater.*, **30** (1994) 975 9.
33. Cotton, J. D., Noebe, R. D. & Kaufman, M. J., *Intermetallics*, **1** (1993) 117 26.
34. Joslin, S. M., PhD. Thesis, University of Tennesse (in progress).
35. Broek, D., *Elementary Engineering Fracture Mechanics*, Martinus Nijhoff, Boston, MA, 1986, p. 115.
36. Chan, K. S., *Met. Trans. A*, **22A** (1991) 2021 9.
37. Cotton, J. D., Noebe, R. D. & Kaufman, M. J., *Intermetallics*, **1** (1993) 3 20.
38. Noebe, R. D., Bowman, R. R. & Nathal, M. V., *Int. Mater. Rev.*, **38** (1993) 193-232.
39. Jackson, K. A. & Hunt, J. D., *Trans. AIME*, **236** (1966) 1129 42.
40. Johnson, D. R., Oliver, B. F., Noebe, R. D. & Whittenberger, J. D., *TMS Fall Meeting*, Pittsburgh, 1993, TMS, Warrendale, PA, (in press).